



**HAL**  
open science

# Large Eddy Simulation of Fluid-Elastic Instability in Square Normal Cylinder Array

Vilas Shinde, Elisabeth Longatte, Franck Baj

► **To cite this version:**

Vilas Shinde, Elisabeth Longatte, Franck Baj. Large Eddy Simulation of Fluid-Elastic Instability in Square Normal Cylinder Array. *Journal of Pressure Vessel Technology*, 2018, 140 (4), pp.041301. 10.1115/1.4040417 . hal-02010667

**HAL Id: hal-02010667**

**<https://hal.science/hal-02010667v1>**

Submitted on 10 Jul 2024

**HAL** is a multi-disciplinary open access archive for the deposit and dissemination of scientific research documents, whether they are published or not. The documents may come from teaching and research institutions in France or abroad, or from public or private research centers.

L'archive ouverte pluridisciplinaire **HAL**, est destinée au dépôt et à la diffusion de documents scientifiques de niveau recherche, publiés ou non, émanant des établissements d'enseignement et de recherche français ou étrangers, des laboratoires publics ou privés.

# Large Eddy Simulation of Fluid-Elastic Instability in Square Normal Cylinder Array

Vilas Shinde, Elisabeth Longatte\*, Franck Baj

IMSIA, Boulevard Gaspard Monge, Paris Saclay University, Palaiseau 91120, France

Large eddy simulations (LES) are performed at low Reynolds number (2000–6000) to investigate the dynamic fluid-elastic instability in square normal cylinder array for a single-phase fluid cross flow. The fluid-elastic instability is dominant in the flow normal direction, at least for all water-flow experiments (Price, S., and Paidoussis, M., 1989, “The Flow-Induced Response of a Single Flexible Cylinder in an in-Line Array of Rigid Cylinders,” *J. Fluids Struct.*, 3(1), pp. 61–82). The instability appears even in the case of single moving cylinder in an otherwise fixed-cylinder arrangement resulting in the same critical velocity (Khalifa, A., Weaver, D., and Ziada, S., 2012, “A Single Flexible Tube in a Rigid Array as a Model for Fluidelastic Instability in Tube Bundles,” *J. Fluids Struct.*, 34, pp. 14–32); Khalifa et al. (2013, “Modeling of the Phase Lag Causing Fluidelastic Instability in a Parallel Triangular Tube Array,” *J. Fluids Struct.*, 43, pp. 371–384). Therefore, in the present work, only a central cylinder out of 20 cylinders is allowed to vibrate in the flow normal direction. The square normal (90 deg) array has 5 rows and 3 columns of cylinders with 2 additional side columns of half wall-mounted cylinders. The numerical configuration is a replica of an experimental setup except for the length of cylinders, which is of 4 diameters in numerical setup against about 8 diameters in the experiment facility. The single-phase fluid is water. The standard Smagorinsky turbulence model is used for the subgrid scale eddy viscosity modeling. The numerical results are analyzed and compared to the experimental results for a range of flow velocities in the vicinity of the instability. Moreover, instantaneous pressure and fluid-force profiles on the cylinder surface are extracted from the LES calculations in order to better understand the dynamic fluid-elastic instability.

## 1 Introduction

Flow-induced vibration in heat exchangers is a subject of major concern, especially in nuclear power plants. The recent advancement of computing power has enabled to perform large-scale numerical simulations and investigate the underlying physics of such complex problems. Flow-induced vibration in cylinder arrangement is characterized by several patterns. It depends on numerous parameters such as arrangement of cylinders, pitch ratio, mass-damping parameter as well as flow turbulence properties. Fluid-elastic instability in tubes array exists in laminar as well as in turbulent flow regimes.

Large amount of research work is performed on this phenomenon to enhance understanding of the stability limit criteria in order to prevent its occurrence. Many theoretical models have been developed since the phenomenon was first brought to notice by Roberts [1] and later by Connors [2]. The models proposed for the phenomenon provide an insight into fluid-elastic instability by means of different instability mechanisms such as “fluid flow jet switching mechanism,” “stiffness-controlled mechanism,” and “damping-controlled mechanism” [3–9]. In general, the theories are developed using empirical relations of the form  $u_c^* = K(m^*\delta)^a$ , where the critical reduced velocity  $u_c^*$  is directly proportional to fractional power  $a$  of the mass-damping parameter defined as the product of the mass ratio and the damping coefficient ( $m^*\delta$ ).  $K$  represents a constant. These empirical relations may be derived from several approaches such as potential flow, quasi-static, or unsteady approaches. In addition, dynamic features of the instability such as phase lag between fluid force and

displacement as well as flow with boundary layer effect are considered while modeling the phenomenon. Although many approaches exist, all fall short individually to predict the phenomenon for wide ranges of parameters.

In addition to experiments, computational fluid dynamics provides a recent possibility to simulate and better understand such phenomena. From an industrial point of view, flow in cylinder arrangement is often at high Reynolds numbers. This gives rise to complex interactions between nonlinear instability due to solid motion and near-wall unsteady turbulence developing around cylinders. In order to correctly take into account these interactions and efficiently predict the unsteady near-wall loads, it is necessary to develop reliable approaches of turbulence macrosimulation to separate effects due to low frequency motion associated with structure response and random effects due to chaotic turbulence.

Turbulence models based on unsteady Reynolds-averaged Navier–Stokes (URANS) approach are derived from the assumptions of turbulence in statistical equilibrium. They tend to underestimate the magnitude of global coefficients characterizing drag and lift. Further, the dynamic coupling between fluid load and cylinder motion has a major effect in the occurrence of fluid-elastic instability, therefore, URANS models may not be appropriate. However, in an industrial context, direct numerical simulation involving a fully numerical modeling of all structure scales is computationally expensive. Large eddy simulation (LES) overcomes the shortcoming of URANS approach by capturing the transient features of the flow physics and, contrary to direct numerical simulation, LES enables the simulation of such problems by modeling the subgrid-scale turbulence. Some of the early works on simulation of flow through tube bundles using LES include the work of Ref. [10]. Later, the work of Refs. [11–13] confirmed the benefits of LES over URANS for tube bundle geometries. Although LES is still not reachable for high Reynolds

---

\*Corresponding author.

numbers as it requires high computational resources, it is suitable for low to moderate Reynolds numbers. Recently, similar benefits of LES were illustrated for simulation of vortex-induced vibrations (VIV) at moderate Reynolds numbers [14].

In the present work, LES is carried out to simulate single-phase fluid cross-flow induced vibration in square normal cylinder arrangements for several gap Reynolds numbers from 2000 to 6000 in order to improve the understanding of fluid-elastic instability. The length of computational domain in the spanwise direction is taken 4 diameter long, which provides enough space for LES vortex dynamics as explained later [14]. Moreover, the flow in tube array develops as it passes downstream through tube rows, therefore, full tube array is considered instead of an elemental cell of the array. In many experiments, it has been observed that the fluid-elastic vibrations are predominant in the flow normal direction, especially in water-flow experiments [15]. Also, there are several studies performed on a single cylinder oscillating in a fixed cylinders arrangement [15–17]. It leads to different critical velocities but of the same order as for the fully flexible array of cylinders. Therefore, the central cylinder is only monitored and allowed to oscillate in the flow normal direction. Although, in some studies [18], the instability is found to be dominant in the inflow direction for a wide range of mass-damping parameters and the critical velocities predicted using a single cylinder in fixed array are overestimated compared to the fully flexible array. Therefore, an elementary configuration is involved in the present work in order to split the physical effects.

The article is organized as follows. First, the experimental and numerical configurations are described with details on the computational methods involved for turbulence and fluid-structure interaction modeling. Then, the results are compared between experiments and LES calculations. Finally, an explanation is proposed for the dynamical instability according to numerical solution analysis.

## 2 Configuration

In the present section, configuration is described and computational methods are presented.

**2.1 Experimental Device.** The experimental setup involves 15 full cylinders placed in a water channel path with 10 half cylinders fixed on the either side walls. The central cylinder is flexibly mounted and can oscillate in the flow normal direction only. All other cylinders are rigidly fixed. Water flows from bottom to top and the central cylinder can vibrate only in the horizontal (flow normal) direction. A picture of experiment is provided in Fig. 1. The same geometry is involved in Ref. [19].

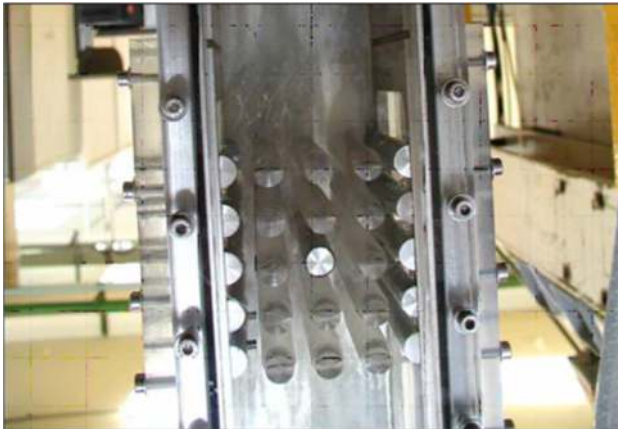


Fig. 1 Experimental device featuring 15 cylinders distributed in 5 rows and 3 columns with 2 additional side columns of half wall-mounted cylinders as described in Ref. [19]

The diameter of each cylinder is  $D = 12.15 \times 10^{-3}$  m. The cylinders are in square normal arrangement with a pitch of  $P = 1.44D$  in both streamwise and flow normal directions. Each cylinder has a mass  $m = 0.298$  kg/m. The channel has a depth of  $100 \times 10^{-3}$  m, the cylinder length is  $L = 100 \times 10^{-3}$  m, and the channel is  $70 \times 10^{-3}$  m wide. Reynolds number is defined by using gap velocity and cylinder diameter. The natural frequency of the central moving cylinder without fluid (i.e., in air) is  $f_n = 14.39$  Hz and the damping ratio is 0.25%.

The vibrations are measured in terms of the strain at the bottom of the monitored tube and recorded during 1000 s. The temporal modal analysis provides the values of damping and frequency of the first predominant mode of the tube vibration.

**2.2 Computational Domain.** The computational domain is  $269.5 \times 10^{-3}$  m long and  $70 \times 10^{-3}$  m wide. The domain extension is about  $5D$  upstream and  $10D$  downstream the cylinder array as shown in Fig. 2. The depth of the channel is  $48.6 \times 10^{-3}$  m. Thus, the length of cylinders is  $4D$  against about  $8D$  in the experimental setup. This approximation results from several considerations extracted from the literature for VIVs of one single cylinder in an infinite medium [14] and extrapolation to confined configurations involving cylinder arrangements [20]. As far as single cylinder VIVs are concerned, the law effect of increasing the length of the domain from  $\pi D$  to  $2\pi D$  is pointed out in Refs. [21] and [22]. Since cross structure length is affected by transition in shear layer [23], it is affected by the near-wake patterns and  $2\pi D$  is not sufficient for capturing length correlations and lift force coherence functions for very long elongation. Simulating long cylinders requires too large domains in the length direction which is not reachable from a computational point of view. Therefore, the  $4D$  length approximation is not sufficient for predicting very long cylinder behavior but it provides results close to a  $8D$  geometry as in the experiment [24]. The same comment can be made for cylinder arrangements due to the correlation of confinement effect and cross structure development [20]. Therefore, the assumption of  $4D$  is reasonable as illustrated in the results below.

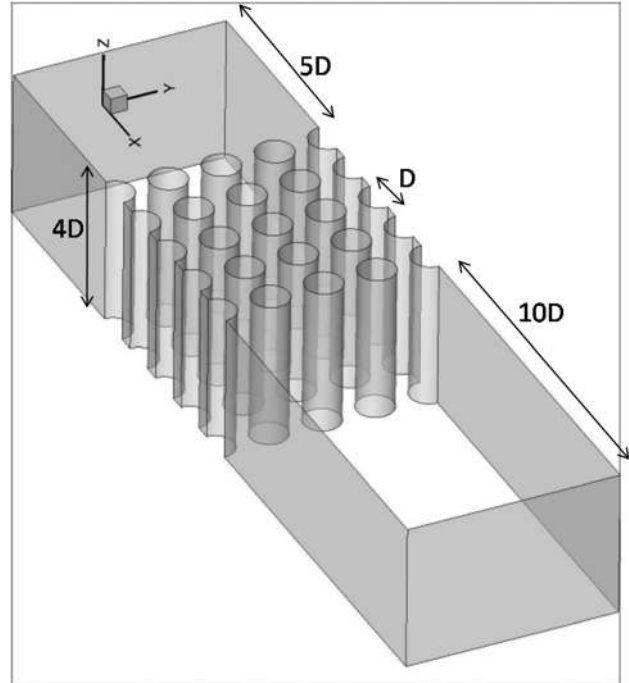
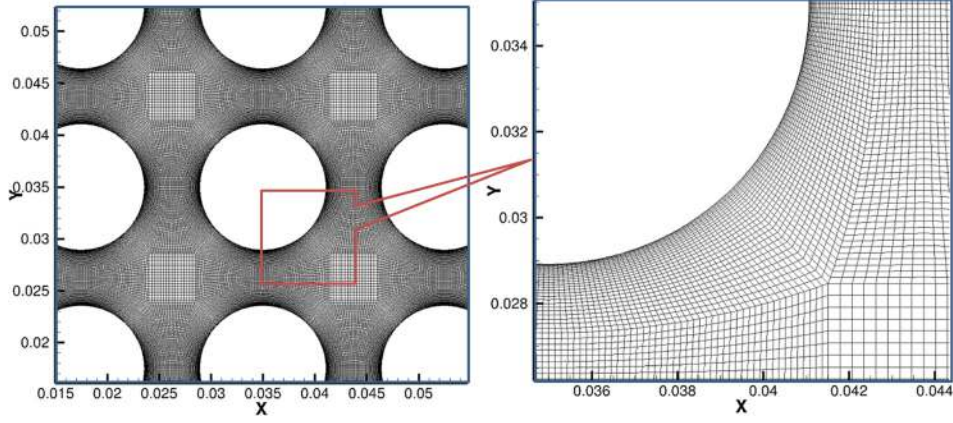


Fig. 2 Geometry of the computational domain with the inflow direction  $Ox$ , the cross flow direction  $Oy$ , and the length direction  $Oz$



**Fig. 3** Near-wall mesh inside the tube array (left). Mesh details close to near-wall region inside the tube array (right).

Thus, using a two-dimensional length is sufficient to have spanwise turbulent flow structures using LES. The pitch ratio is 1.44 with square normal arrangement of the cylinders as in the experimental configuration. Mechanical properties are defined according to experiment parameters for fluid, solid, and geometry too.

The computational domain is discretized by using a structured grid. The mesh involves about  $25.3 \times 10^6$  cells to ensure that the near-wall mesh refinement conditions are satisfied ( $y^+$  less than 1) as shown in Fig. 3. The perimeter of cylinders is divided into 360 cells, while the first layer of computational cells is at a distance of  $1.8 \times 10^{-5}$  m along the cylinder wall. The cells have expansion ratio of 1.2 along the wall normal direction. The mesh is relatively coarser ( $2 \times 10^{-3}$  m) far downstream in the wake region. The mesh topology is built to optimize the compromise between accuracy of near-wall resolution of flow fields and performance capability.

**2.3 Turbulence Modeling and Solution Method.** In LES, the large-scale structures from the fluid flow are directly captured, whereas the smallest ones are modeled. The small scale turbulent motion is assumed to be isotropic and simple Boussinesq type relations are employed to model the filtered turbulence. In the present work, standard Smagorinsky's subgrid scale eddy viscosity model is used since it was reported in Refs. [11] and [25] that the subgrid scale model has a little influence on the results. The incompressible Navier–Stokes equations in filtered form can be written as follows:

$$\begin{aligned} \frac{\partial \tilde{u}_i}{\partial x_i} &= 0 \\ \frac{\partial \tilde{u}_i}{\partial t} + \tilde{u}_j \frac{\partial \tilde{u}_i}{\partial x_j} &= -\frac{1}{\rho} \frac{\partial \tilde{p}}{\partial x_i} + \frac{\partial}{\partial x_j} \left[ (\nu + \nu_t) \left( \frac{\partial \tilde{u}_i}{\partial x_j} + \frac{\partial \tilde{u}_j}{\partial x_i} \right) \right] \end{aligned} \quad (1)$$

$\tilde{u}_i$  is the filtered velocity component in direction  $i$ .  $\rho$ ,  $\nu$ , and  $\nu_t$  are density, kinematic viscosity, and turbulent kinematic viscosity, respectively.  $t$  and  $x_i$  represent time and space, respectively. The filtered pressure  $\tilde{p}$  includes the trace of the subgrid scale stress tensor  $\tau_{ij}$ , which is given by the following equation:

$$\tau_{ij} = -2\nu_t \tilde{S}_{ij} + \frac{1}{3} \tau_{kk} \delta_{ij} \quad (2)$$

Smagorinsky's model provides a value of subgrid scale turbulent viscosity  $\nu_t$ . It is a Boussinesq type eddy viscosity relation given by the following equation:

$$\nu_t = (C_s l_g)^2 \sqrt{2\tilde{S}_{ij}\tilde{S}_{ij}} \quad (3)$$

$l_g$  is the length scale which is the size of grid cells,  $\tilde{S}_{ij}$  is the strain rate tensor while  $C_s$  represents Smagorinsky's constant. The value of  $C_s$  varies with the type of turbulence. In shear flows, it is about 0.1 against higher value 0.18 for high Reynolds number flows.

For computations on SuperComputers, a co-located finite volume method is involved with a second-order central difference scheme for the space discretization and a second-order Crank–Nicolson scheme for time steps. At first, the physical properties are calculated. The velocity field is computed in a predictor step followed by a correction step to take into account the pressure equation implicitly [26].

The inlet of computation domain is Dirichlet boundary condition with specified constant inflow velocity. The outlet corresponds to homogeneous Neumann boundary condition for velocity, while a Dirichlet boundary condition for pressure is employed at outlet such that  $(\partial^2 P / \partial n \partial \tau = 0)$  for any vector  $\tau$  colinear with outlet.  $P$  is the pressure and  $n$  is normal to boundary face. The side walls with cylinders half-mounted have a no-slip wall boundary condition while as periodic boundary condition is employed for the domain closures in the  $z$  direction. Static case simulations are carried out until the flow is established for each reduced velocity and provide an initialization for dynamic case simulations. Then, dynamical interaction between the central moving cylinder and the flow takes place. The simulations are performed for about 2 times the residence time in static configuration, with all cylinders fixed. Once the flow is established, the central cylinder is set for fluid-structure interaction using a moving-mesh pseudo-eulerian method. A constant time-step of  $2 \times 10^{-4}$  s is used for all simulations. The simulations are performed for 40 s in dynamic case, which is about 400 times the natural frequency of cylinder in water and about 20 times the flow residence time.<sup>2</sup>

**2.4 Fluid-Structure Interaction.** The vibration of cylinder is coupled with fluid load by means of an iterative procedure. To reproduce real experiment, the external force of gravity is also considered, although it has no influence on the instability. Since the central cylinder is rigid and flexibly mounted, a simple ordinary differential equation for motion of a single degree-of-freedom is fitted with the dynamic unsteady fluid load as displayed in Fig. 4.

Therefore, the cylinder response is solution of the following equation:

$$m \frac{d^2 y}{dt^2} + c \frac{dy}{dt} + ky = F_y \quad (4)$$

<sup>2</sup>LES computations are performed by using Code–Saturne on 768 MPI-cores of computational processor units (CPU) which are Intel(R) Xeon(R) processors with speed 2.93 GHz [26].

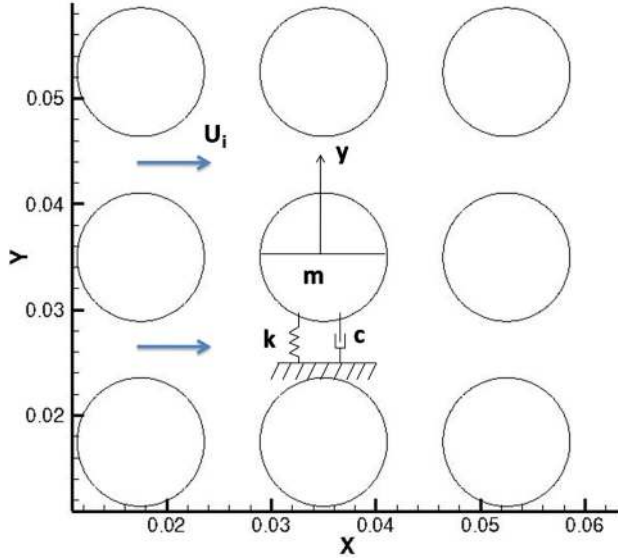


**Fig. 4 Schematic of the fluid-structure coupling for the central moving cylinder**

$F_y$  is the fluid load in the flow normal direction,  $y$  is the displacement of the cylinder in the same direction.  $c$  and  $k$  are, respectively, the structural damping and stiffness coefficients of the cylinder related to the natural frequency  $f_n$  and damping ratio  $\zeta$  as  $k = (2\pi f_n)^2 m$  and  $c = 2\zeta\sqrt{mk}$ .

Equation (4) is solved using Newmark HHT algorithm. It uses fluid force ( $F_y$ ) to estimate the displacement ( $y$ ). The updated position of cylinder is used for fluid mesh actualization and next flow iteration. The Poisson equation is solved for moving mesh in an elliptic framework which is convenient in a small displacement context. An artificial mesh viscosity is used to control the near-wall cell deformations.

### 3 Results

**3.1 Comparison.** The experimental results are tabulated in Table 1. The first column is volumetric flow of water through the channel (in l/s). Columns 2 and 3 are intertube velocity in m/s and intertube Reynolds number, respectively. The last column is the response frequency ( $f_n$ ) of the central cylinder in Hz. The damping ratio ( $\zeta$ ) tends to zero as the cylinder reaches stability limit. In experiment, the maximum volume flow rate achieved is 1 l/s, for a value of damping ratio ( $\zeta$ ) close to zero (0.05%). This gives a maximum gap velocity of 0.467 m/s onset of the fluid-elastic instability.

The experimental data enlisted (in Table 1) correspond to the LES carried out at various reduced velocities ( $u^*$ ). The reduced velocity is defined as  $u^* = u_i/(f_n D)$ , where  $f_n$  is the natural frequency of cylinder in air (here 14.39 Hz). A time-domain modal analysis is performed using a statistical method of maximum-likelihood estimation. The characteristic modes are predefined by means of a characteristic function. The parameters of the

**Table 1 Experimental results**

$Q$ (lit/s)	$u_i$ (m/s)	$Re_i$	$f_n$ (Hz)
0.35	0.164	1988	11.86
0.45	0.210	2556	11.71
0.55	0.257	3124	11.93
0.65	0.304	3692	11.91
0.75	0.351	4260	11.62
0.85	0.397	4828	11.57
0.95	0.444	5396	11.55

**Table 2 Numerical results**

$u^*$	$u_i$ (m/s)	$Re_i$	$f_n$ (Hz)
1.00	0.175	2124	11.80
1.25	0.219	2655	11.05
1.50	0.262	3186	11.45
1.75	0.306	3717	12.15
2.00	0.350	4248	10.96
2.25	0.393	4779	11.30
2.50	0.437	5310	11.46

characteristic function are treated using a Quasi-Newton type method for nonlinear optimization. In addition, Prony's method is used to provide an initialization for the nonlinear optimization of the parameters of characteristic function. Thus, the modal analysis provides the modal frequency and damping ratio of the random response of the cylinder.

Table 2 shows the results of LES for several intertube reduced velocities. The values of reduced velocity are listed in the first column. The second and third columns contain the intertube velocity  $u_i$  and Reynolds number ( $Re_i$ ), respectively. The response frequency ( $f_n$ ) of the cylinder at different reduced velocities is listed in the fourth column.

The numerical time response signals are short for the accurate statistical analysis of damping ratio ( $\zeta$ ) except for a reduced velocity  $u^* = 2.00$ . The damping ratio estimated using the response of cylinder in LES at  $u^* = 2.00$  is 2.05% against an experimental value of 2.37%. The response frequency (in experiment, Table 1) shows a slight decrease at  $u^* \approx 1.25$  and a sudden increase at  $u^* \approx 1.50$ . It is followed by a monotonous decrease up to reduced velocity  $u^* \approx 2.50$ . Similarly, in LES calculations, the response frequency (Table 2) observes a decrease at  $u^* = 1.25$  but a gradual increase up to  $u^* = 1.75$ . The trend slightly differs after a sudden decrease at the reduced velocity of  $u^* = 2.00$  (Fig. 5 shows the comparison).

Although, the experiments are carried out at low range of Reynolds numbers (2000–6000), the time response of the cylinder oscillations is already chaotic and modulated. Figure 6 shows comparison between the time signals of vibration in central cylinder for the LES (top) and experiment (bottom).

Figure 7 shows power spectral density (PSD) of the signals displayed in Fig. 6. The spectra show distinct peaks at about the natural frequency of the cylinder in water for both, LES and experiment solutions.

**3.2 Analysis.** The theoretical development on fluid-elastic instability has been studied by many researchers by modeling

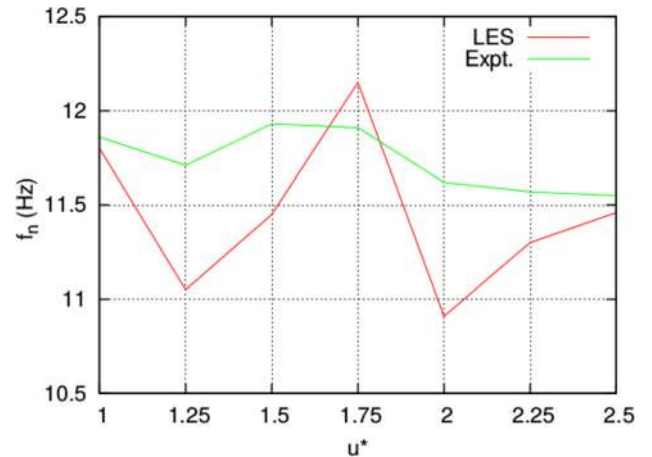


**Fig. 5 Comparison of the modal frequency of cylinder response: LES versus experiment**

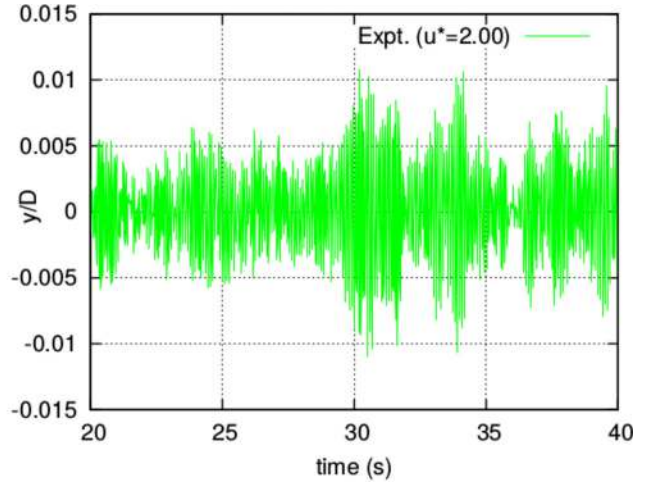
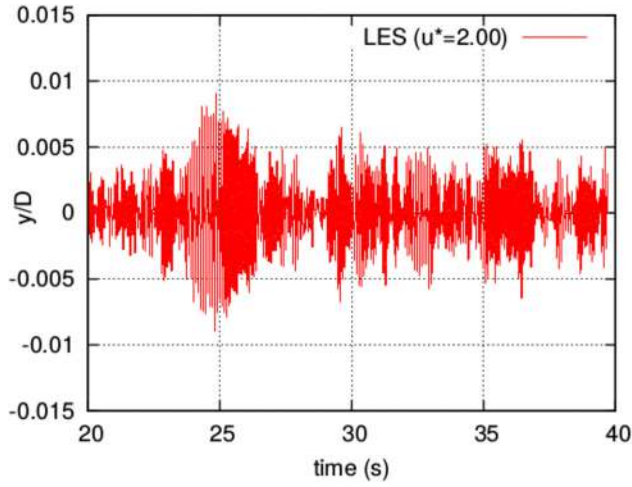


Fig. 6 Response of the central cylinder at  $u^* = 2.00$ : numerical (left) versus experimental (right) signals

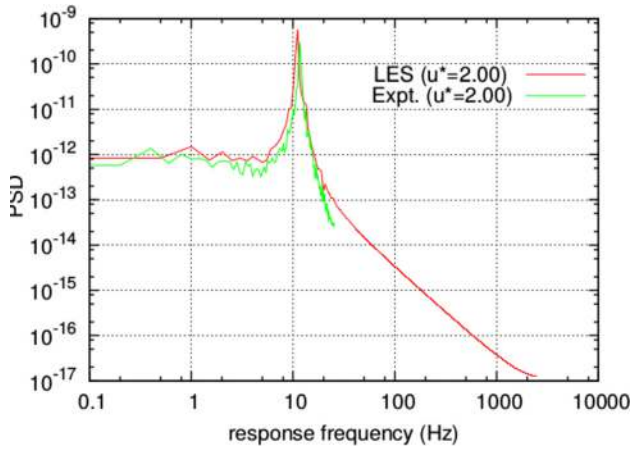


Fig. 7 Power spectral density of the cylinder response at reduced velocity  $u^* = 2.00$ : numerical ( $0.1 \leq f_n$  ( $0.1 \leq 2000$ ) versus experimental ( $0.1 \leq f_n \leq 20$ ) spectra

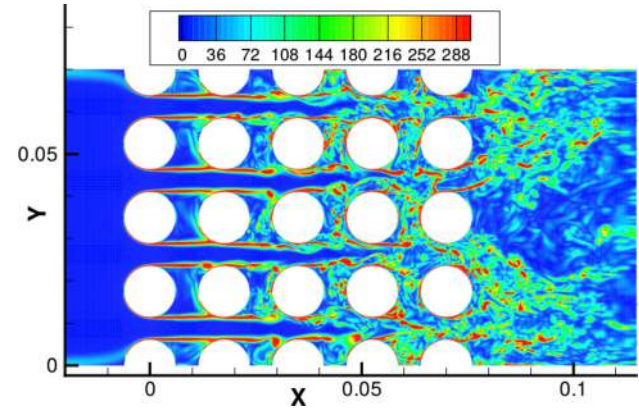


Fig. 8 An instantaneous vorticity (absolute) plot at reduced velocity  $u^* = 2.00$

different mechanisms [2,3,5,6,8,9,15]. All theories are based on empirical relations and the fluid force coefficients measured experimentally. Further, no unique theory holds good for all range of parameters, indicating the deceptive nature of the instability. In spite of the ambiguous nature of the instability, some features are commonly observed about the instability such as the dominance of vibrations in the flow normal direction. The phase lag between fluid force and cylinder displacement is often considered as an important parameter too Refs. [16] and [17]. In this section, we analyze the results to better understand fluid flow through the array and fluid force on the surface of the monitored vibrating central cylinder.

Figure 8 shows an instantaneous vorticity magnitude field at a mid-plane in the LES computational domain. The turbulence in the flow gradually develops through the cylinders array. The shear layers formed at first row of cylinders (inline cylinders with same  $X$  coordinate) start breaking down after second row, resulting in increased level of turbulence through the tube array.

The flow periodicity, or shear layer vortex shedding, attachment and separation of the flow on the cylinder surface plays an important role [18,27] in the fluid-elastic instability. The time-averaged pressure profile on the surface of oscillating cylinder is shown in Fig. 10. The pressure profile shows two maxima and two minima in the azimuthal direction ( $\theta$ ). It infers that the length of the flow structures in the  $Z$  direction is approximately  $2.5D$ . The pressure profile shows asymmetry about  $\theta = 180$  deg in the plot. This

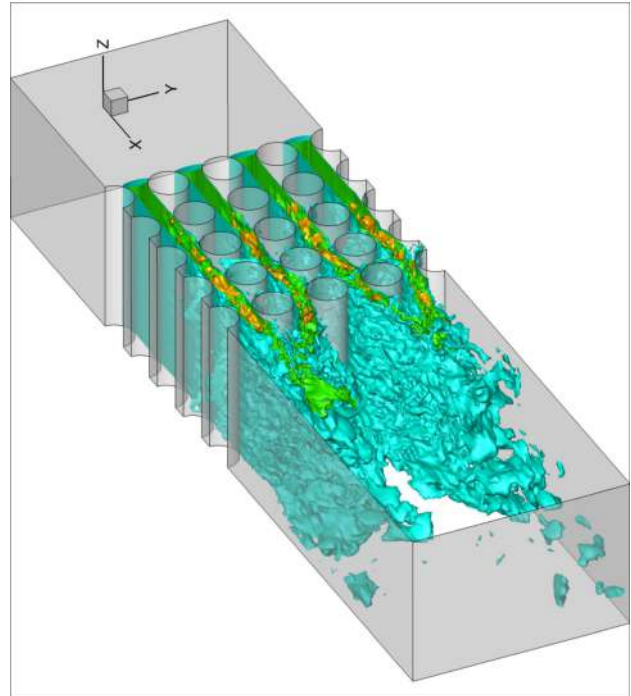
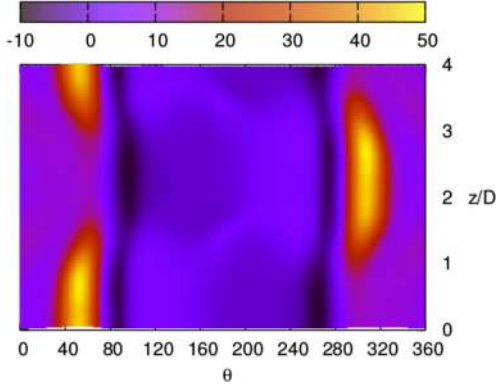


Fig. 9 Iso-surfaces of the instantaneous velocity (magnitude, m/s) at 0.2 (large spread region), 0.3 (interstitial regions), and 0.4 (localised interstitial regions)



**Fig. 10** The time-averaged pressure (Pa) profile on the cylinder surface at  $u^* = 2.00$

could be attributed to “flipping” of the fluid flow at a fairly low frequency as observed experimentally by Mahon and Meskell [27,28]. The time-length averaged pressure and total force in the  $Y$  direction ( $F_y$ ) on the cylinder surface is plotted in Fig. 11. Clearly, it is indicating two locations for attachment ( $\theta \approx 55\text{deg}$  and  $\theta \approx 305\text{deg}$ ) of the flow and two locations for separation ( $\theta \approx 90\text{deg}$  and  $\theta \approx 270\text{deg}$ ) of the flow on the surface of the cylinder.

The fluid-elastic instability is known to occur with a self-excitation mechanism. The motion of the cylinder disturbs the flow field around, and in response, the fluid forces further increase the vibration in cylinder. The transient development of the instability is difficult to visualize experimentally, in terms of the fluid forces and displacement, hence less understood. These transient interactions are considered in theoretical models in terms of phase lag between the fluid force and the displacement as well as temporal variation of the boundary layer of the cylinder. In Fig. 12, we shed light on the time evolution of pressure profile on the cylinder surface at all reduced velocities considered for analysis. The time duration considered is about one period of the cylinder oscillations (i.e.,  $\sim 0.1$  s)

The time varying instantaneous pressure on the cylinder surface is shown in Fig. 12. The subplots show influence of increasing reduced velocity on the pressure. The pressure magnitudes observed increase from  $u^* = 1.00$  up to  $u^* = 1.50$ . It decreases for reduced velocity  $u^* = 1.75$  and follows a monotonous increase thereafter. The changing pressure magnitudes are also accompanied with change in the time-evolved pressure profiles at each reduced velocity. The pressure time-evolutions for one period of cylinder oscillation (Fig. 12) are either symmetric ( $u^* = 1.00$ ,  $u^* = 1.75$ , and  $u^* = 2.00$ ) or nearly antisymmetric ( $u^* = 1.25$ ,  $u^* = 1.50$ ,  $u^* = 2.25$ , and  $u^* = 2.50$ ). This indicates

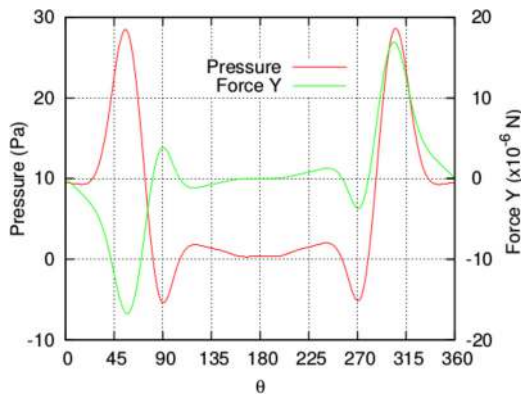


**Fig. 11** The azimuthal pressure and total force (in the  $Y$  direction) profiles (time-length averaged)

the way fluid force acts on the cylinder surface changes with increasing reduced velocity. The symmetrical pressure profiles (such as  $u^* = 1.00$ ,  $u^* = 1.75$ , and  $u^* = 2.00$  in Fig. 12) imply that the adjacent flow streams exert a balanced force on the cylinder at the same time, thus limiting its movement. On the contrary, in case of the reduced velocities  $u^* = 1.25$ ,  $u^* = 1.50$ ,  $u^* = 2.25$ , and  $u^* = 2.50$ , the time evolution of the pressure is not symmetrical. The adjacent flow streams exert an unbalanced force on the cylinder at a time, resulting in higher amplitudes of the vibration. The increase or decrease of the vibration amplitudes is also associated with the change in response frequency ( $f_n$ ) of the cylinder in Fig. 5. The response frequency ( $f_n$ ) decreases up to reduced velocity  $u^* = 1.25$ , then follows an increase up to reduced velocity  $u^* = 1.75$ . The trend tends to differ (in experiment with numerical results) for higher values of reduced velocity.

The difference in the time-evolving pressure profiles from Fig. 12 can be correlated to the instantaneous flow field at reduced velocities  $u^* = 2.00$  and  $u^* = 2.25$ . Figure 13 shows the instantaneous velocity fields at  $u^* = 2.00$  (top) and  $u^* = 2.25$  (bottom). The flow streams adjacent to the central oscillating cylinder observe a high velocity patch whenever the cylinder is displaced toward it. The high velocity patches are marked in Fig. 13 on the adjacent flow streams of the oscillating cylinder. These high velocity disturbances caused by the cylinder movement are carried downstream with the flow. The high velocity patches shown for the reduced velocity  $u^* = 2.00$  (Fig. 13 top) show symmetry in appearance on the flow channels. In contrast, at reduced velocity  $u^* = 2.25$  (Fig. 13 bottom), the high velocity patches on the flow streams appear alternatively, resulting in the antisymmetrical time evolution of the pressure profile on the cylinder surface.

Figure 9 shows a three-dimensional velocity plot at reduced velocity  $u^* = 2.00$ . It shows the iso-surfaces of instantaneous velocity at 0.2 m/s (in aqua color), 0.3 m/s (in green color), and 0.4 m/s (in brown color).

**3.3 Comparison Between Static and Dynamic Configurations.** The comparison is done using the spectra of  $Y$  velocity ( $u_2$ ) at probe locations  $P1$  and  $P3$  for increasing reduced velocity ( $u^*$ ). Furthermore, the velocity spectra at these upstream and downstream locations are compared with the spectrum of cylinder vibration ( $y$ ) in Fig. 14. In the static case simulations, the red curves in Figs. 14(a) and 14(b), the shear layer frequency at gap reduced velocity  $u^* = 1.00$  is  $f_{sh}^* = 0.56$ . There are higher harmonics of this frequency in the spectra computed at the downstream location  $P3$ . In the dynamic case computations, the green curves in Figs. 14(a) and 14(b), there appears an extra frequency peak at both the upstream and downstream locations, which corresponds to the response frequency of cylinder. On the other hand, the response spectrum of cylinder, the blue curve in Figs. 14(a) and 14(b), shows a peak at  $f^* = 0.56$ . Figures 14(c) and 14(d) show similar comparison for the intertube reduced velocity  $u^* = 1.50$ . The red curves of the static case simulations show two frequency peaks, one at 0.79 and its first harmonic at about 1.63, at both  $P1$  and  $P2$  locations. On the contrary, the velocity spectra in the dynamic case (green curves in Figs. 14(c) and 14(d)) show a distinct frequency at the cylinder response frequency ( $f_n^* = 1$ ). Furthermore, the cylinder response spectrum at this reduced velocity  $u^* = 1.50$  is elevated, in terms of the spectral power, compared to the response spectra at both  $u^* = 1.23$  and  $u^* = 2.47$  reduced pitch velocities, which may be due to a possible synchronization between the shear layer frequencies and the cylinder response frequency. The flow velocity spectra at the gap velocity  $u^* = 2.00$  show wider peaks at frequency 1.92, at the upstream ( $P1$ ) location only. The frequency peak corresponding to the cylinder vibration is not distinctly reflected in the velocity spectra (Figs. 14(e) and 14(f)). The shear layer frequencies increase with further increase in the Reynolds number. The fluid-elastic instability in the dynamic calculations occurs at Reynolds number  $Re_p = 5310$ , where the flow frequency at the upstream locations

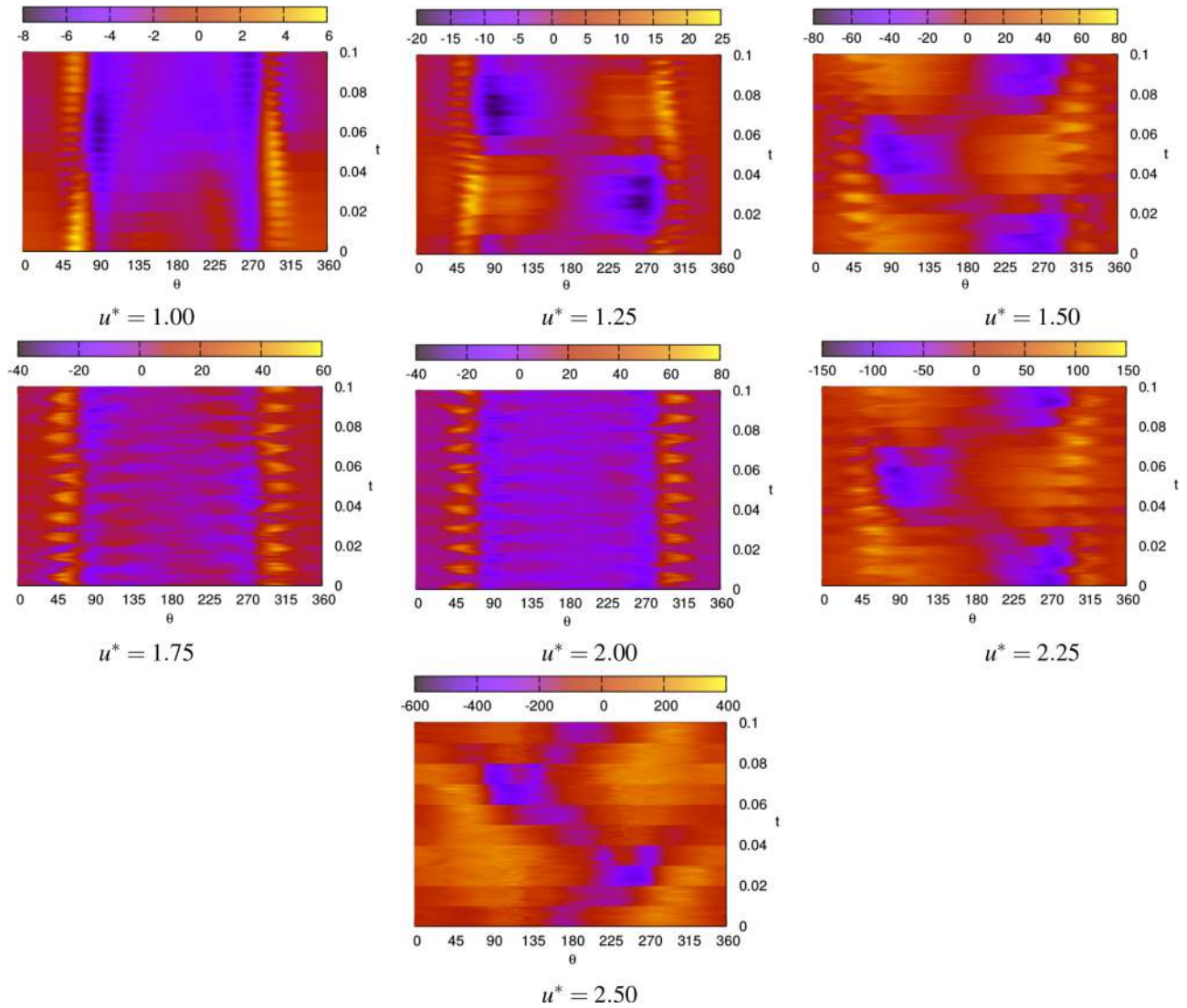


Fig. 12 The instantaneous pressure (Pa) profiles on the cylinder surface, evolving with time for approximately one period of its frequency at various reduced velocities ( $u^*$ ):  $u^* = 1.00$ ,  $u^* = 1.25$ ,  $u^* = 1.50$ ,  $u^* = 1.75$ ,  $u^* = 2.00$ ,  $u^* = 2.25$ ,  $u^* = 2.50$

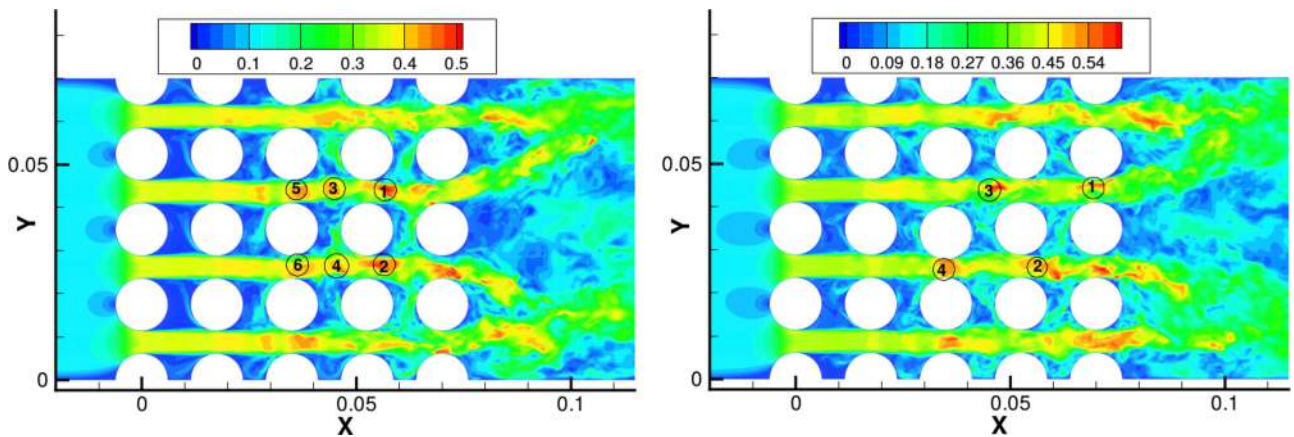
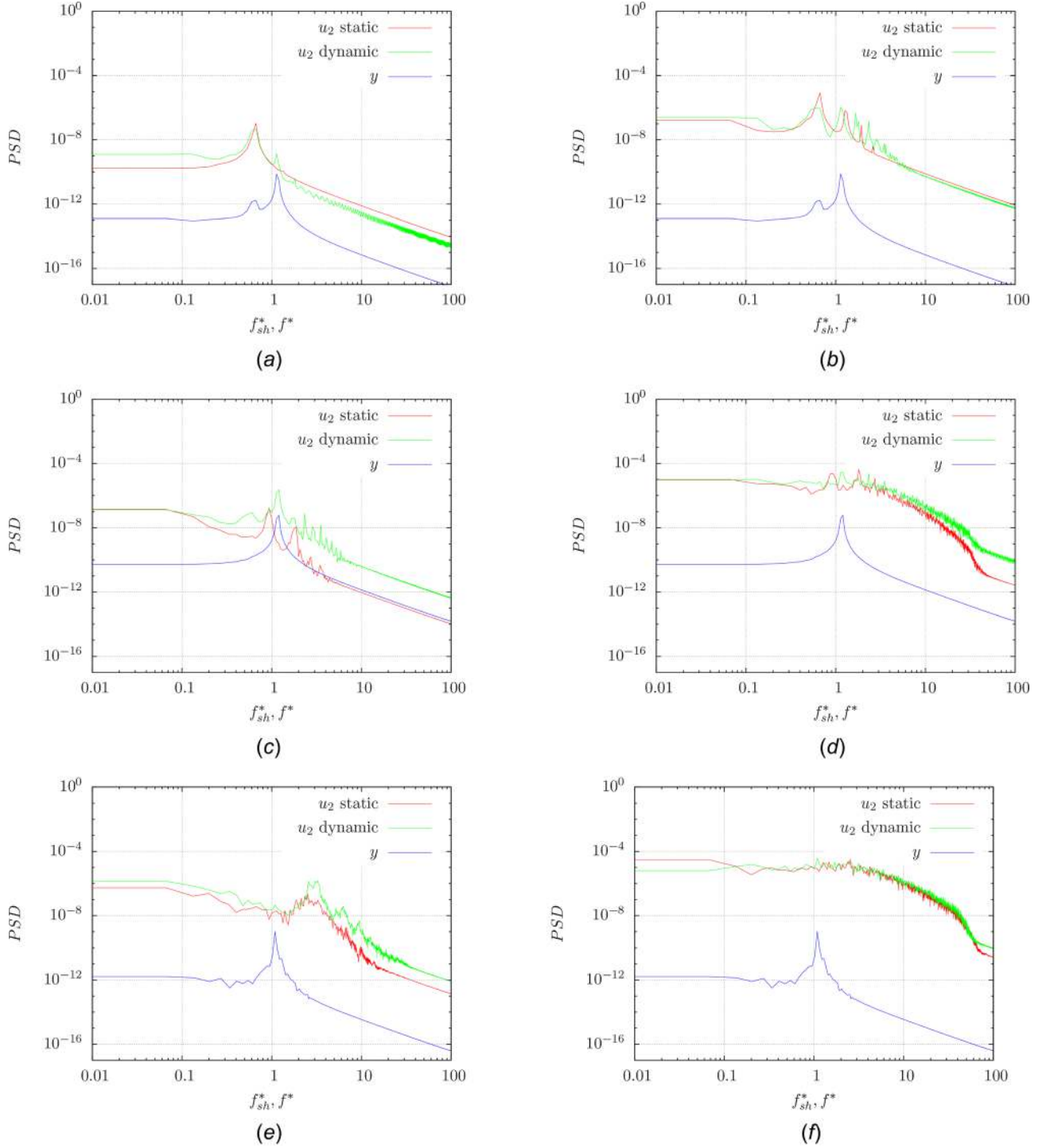


Fig. 13 The instantaneous velocity fields at  $u^* = 2.00$  and  $u^* = 2.25$ , depicting the correspondence with the time evolution of pressure profiles in Fig. 12



**Fig. 14** Power spectral densities of Y velocity in static and dynamic cases at an upstream (P1) and a downstream (P3) location, respectively, upstream and downstream the moving cylinder, in comparison with the cylinder response spectrum for increasing reduced velocity: (a) location P1,  $u^* = 1$ ; (b) location P3,  $u^* = 1$ ; (c) location P1,  $u^* = 1.50$ ; (d) location P3,  $u^* = 1.50$ ; (e) location P1,  $u^* = 2.00$ ; and (f) location P3,  $u^* = 2.00$

(P1, P2) is about 3.3 with no distinct frequency peaks at the downstream locations (P3, P4). Therefore, the mechanism of the fluid-elastic instability must be different from the classical “lock-in” phenomenon.

#### 4 Conclusion

Large eddy simulation carried out to study fluid structure interaction in an in-line cylinder array. An arbitrary-Lagrangian-Eulerian (ALE) approach is adapted to simulate the

coupling of fluid flow and motion of cylinder. The root-mean-squared displacement, time response of the cylinder vibration, the PSD as well as the damping ratio show a good agreement with the experimental results for reduced velocity  $u^* = 2.00$ . In addition, the response frequencies of the cylinder for the range of reduced velocities are in agreement with the experimental values of the frequencies. This shows that the dynamic unsteady interactions between fluid load and cylinder vibration are well captured by LES. Turbulence develops gradually as the flow passes downstream through tube rows. The intertube fluid flow has the

attachment location at an azimuthal angle of  $\approx 55$  deg ( $\approx 306$  deg on the other side) on the cylinder and a separation point at  $\approx 90$  deg ( $\approx 270$  deg on the other side). In the analysis, we shed some light on the dynamic interactions of the cylinder vibration and the adjacent flow streams. The time evolution of the pressure profiles on the cylinder surface is indeed linked with flow stream perturbations induced by the cylinder vibration.

## Acknowledgment

The authors would like to thank the French Scientific National Research Center (CNRS) and the French Energy company (EDF) for the computing facilities and the Atomic Energy Commission (CEA) for the experimental results. This work was supported by the ANR project BARESAFE on Safety Barrier Reliability Optimization through Numerical Simulation.

## References

- [1] Roberts, B. W., 1966, *Low Frequency, Aerolastic Vibrations in a Cascade of Circular Cylinders*, Institution of Mechanical Engineers, Westminster, UK.
- [2] Connors, H., 1970, "Fluidelastic Vibration of Tube Arrays Excited by Cross Flow," ASME Paper No. 42-56.
- [3] Blevins, R., 1974, "Fluid Elastic Whirling of a Tube Row," *ASME J. Pressure Vessel Technol.*, **96**(4), pp. 263-267.
- [4] Tanaka, H., and Takahara, S., 1981, "Fluid Elastic Vibration of Tube Array in Cross Flow," *J. Sound Vib.*, **77**(1), pp. 19-37.
- [5] Chen, S., 1983, "Instability Mechanisms and Stability Criteria of a Group of Circular Cylinders Subjected to Cross-Flow—Part I: Theory," *J. Vib., Acoust., Stress, Reliab. Des.*, **105**(2), pp. 51-58.
- [6] Chen, S., 1983, "Instability Mechanisms and Stability Criteria of a Group of Circular Cylinders Subjected to Cross-Flow—Part 2: Numerical Results and Discussions," *J. Vib., Acoust., Stress, Reliab. Des.*, **105**(2), pp. 253-260.
- [7] Paidoussis, M. P., and Price, S., 1989, "The Mechanisms Underlying Flow-Induced Instabilities of Cylinder Arrays in Cross-Flow," *Design & Analysis*, Elsevier, New York, pp. 147-163.
- [8] Lever, J., and Weaver, D., 1982, "A Theoretical Model for Fluid-Elastic Instability in Heat Exchanger Tube Bundles," *ASME J. Pressure Vessel Technol.*, **104**(3), pp. 147-158.
- [9] Granger, S., and Paidoussis, M., 1996, "An Improvement to the Quasi-Steady Model With Application to Cross-Flow-Induced Vibration of Tube Arrays," *J. Fluid Mech.*, **320**(1), pp. 163-184.
- [10] Hassan, Y., and Barsamian, H., 2004, "Tube Bundle Flows With the Large Eddy Simulation Technique in Curvilinear Coordinates," *Int. J. Heat Mass Transfer*, **47**(14-16), pp. 3057-3071.
- [11] Rollet-Miet, P., Laurence, D., and Ferziger, J., 1999, "Les and Rans of Turbulent Flow in Tube Bundles," *Int. J. Heat Fluid Flow*, **20**(3), pp. 241-254.
- [12] Benaouicha, M., Baj, F., and Longatte, E., 2017, "An Algebraic Expansion of the Potential Theory for Predicting Dynamic Stability Limit of in-Line Cylinder Arrangement Under Single-Phase Fluid Cross-Flow," *J. Fluids Struct.*, **72**, pp. 80-95.
- [13] Liang, C., and Papadakis, G., 2007, "Large Eddy Simulation of Cross-Flow Through a Staggered Tube Bundle at Subcritical Reynolds Number," *J. Fluids Struct.*, **23**(8), pp. 1215-1230.
- [14] Jus, Y., Longatte, E., Chassaing, J.-C., and Sagaut, P., 2014, "Low Mass-Damping Vortex-Induced Vibrations of a Single Cylinder at Moderate Reynolds Number," *ASME J. Pressure Vessel Technol.*, **136**(5), p. 051305.
- [15] Price, S., and Paidoussis, M., 1989, "The Flow-Induced Response of a Single Flexible Cylinder in an in-Line Array of Rigid Cylinders," *J. Fluids Struct.*, **3**(1), pp. 61-82.
- [16] Khalifa, A., Weaver, D., and Ziada, S., 2012, "A Single Flexible Tube in a Rigid Array as a Model for Fluidelastic Instability in Tube Bundles," *J. Fluids Struct.*, **34**, pp. 14-32.
- [17] Khalifa, A., Weaver, D., and Ziada, S., 2013, "Modeling of the Phase Lag Causing Fluidelastic Instability in a Parallel Triangular Tube Array," *J. Fluids Struct.*, **43**, pp. 371-384.
- [18] Kevlahan, N.-R., 2011, "The Role of Vortex Wake Dynamics in the Flow-Induced Vibration of Tube Arrays," *J. Fluids Struct.*, **27**(5-6), pp. 829-837.
- [19] Longatte, E., and Baj, F., 2014, "Physical Investigation of Square Cylinder Array Dynamical Response Under Single-Phase Cross-Flow," *J. Fluids Struct.*, **47**, pp. 86-98.
- [20] Berland, J., Deri, E., and Adobes, A., 2014, "Large-Eddy Simulation of Cross-Flow Induced Vibrations of a Single Flexible Tube in a Normal Square Tube Array," *ASME Paper No. PVP2014-28369*.
- [21] Kravchenko, A. G., and Moin, P., 2000, "Numerical Studies of Flow Over a Circular Cylinder at  $Re_d = 3900$ ," *Phys. Fluids*, **12**(2), pp. 403-417.
- [22] Breuer, M., 1998, "Large Eddy Simulation of the Subcritical Flow past a Circular Cylinder: Numerical and Modeling Aspects," *Int. J. Numer. Methods Fluids*, **28**(9), pp. 1281-1302.
- [23] Ma, X., Karamanos, G.-S., and Karniadakis, G., 2000, "Dynamics and Low-Dimensionality of a Turbulent Near Wake," *J. Fluid Mech.*, **410**, pp. 29-65.
- [24] Wissink, J., and Rodi, W., 2008, "Numerical Study of the Near Wake of a Circular Cylinder," *Int. J. Heat Fluid Flow*, **29**(4), pp. 1060-1070.
- [25] Benhamadouche, S., and Laurence, D., 2002, "Les, Coarse Les, and Transient Rans Comparisons on the Flow Across a Tube Bundle," *Engineering Turbulence Modelling and Experiments 5*, Elsevier, New York, pp. 287-296.
- [26] Archambeau, F., Méchitoua, N., and Sakiz, M., 2004, "Code Saturne: A Finite Volume Code for the Computation of Turbulent Incompressible Flows-Industrial Applications," *Int. J. Finite Vol.*, **1**(1), pp. 1-63.
- [27] Anderson, B., Hassan, M., and Mohany, A., 2014, "Modelling of Fluidelastic Instability in a Square Inline Tube Array Including the Boundary Layer Effect," *J. Fluids Struct.*, **48**, pp. 362-375.
- [28] Mahon, J., and Meskell, C., 2012, "Surface Pressure Survey in a Parallel Triangular Tube Array," *J. Fluids Struct.*, **34**, pp. 123-137.
- [29] Mahon, J., and Meskell, C., 2009, "Surface Pressure Distribution Survey In Normal Triangular Tube Arrays," *J. Fluids Struct.*, **25**(8), pp. 1348-1368.